

NLO QCD corrections to W boson production with a massive b -quark jet pair at the Fermilab Tevatron $p\bar{p}$ collider

F. Febres Cordero* and L. Reina†

Physics Department, Florida State University, Tallahassee, FL 32306-4350, USA

D. Wackerroth‡

Department of Physics, SUNY at Buffalo, Buffalo, NY 14260-1500, USA

(Dated: July 18, 2018)

Abstract

We calculate the Next-to-Leading Order (NLO) QCD corrections to $Wb\bar{b}$ production including full bottom-quark mass effects. We study the impact of NLO QCD corrections on the total cross section and invariant mass distribution of the bottom-quark jet pair at the Fermilab Tevatron $p\bar{p}$ collider. We perform a detailed comparison with a calculation that considers massless bottom quarks. We find that neglecting bottom-quark mass effects overestimates the NLO total cross-section for $Wb\bar{b}$ production at the Tevatron by about 8% independent of the choice of renormalization and factorization scale.

*Electronic address: ffebres@hep.fsu.edu

†Electronic address: reina@hep.fsu.edu

‡Electronic address: dow@ubpheno.physics.buffalo.edu

I. INTRODUCTION

The associated production of a W boson with a $b\bar{b}$ pair plays a critical role at the Fermilab Tevatron $p\bar{p}$ collider, since it accounts for one of the most important background processes to both the associated production of a Higgs boson with a W boson, $p\bar{p} \rightarrow HW$ (with $H \rightarrow b\bar{b}$) [1, 2, 3, 4, 5], and single-top production, $p\bar{p} \rightarrow t\bar{b}, \bar{t}b$ (with $t(\bar{t}) \rightarrow Wb(\bar{b})$) [6, 7, 8]. These two processes are of extreme relevance to the physics program of the Tevatron: they both test fundamental predictions of the Standard Model (SM), i.e. the existence of a Higgs boson and the structure of the Wtb vertex, and at the same time constitute a window to new physics. The cross section for $p\bar{p} \rightarrow HW$ has been calculated including up to Next-to-Next-to-Leading (NNLO) QCD corrections [9, 10, 11] and $O(\alpha)$ electroweak corrections [12], while single-top production has been calculated at Next-to-Leading (NLO) in QCD [13, 14, 15, 16, 17, 18, 19, 20, 21], and at one-loop of electroweak (SM and MSSM) corrections [22].

The production of a Higgs boson in association with an electroweak gauge boson, $p\bar{p} \rightarrow HV$ ($V = Z, W$) with $H \rightarrow b\bar{b}$, is the most sensitive production channel of a SM Higgs boson at the Tevatron for a Higgs boson lighter than about 140 GeV. A relatively light SM Higgs boson is preferred by electroweak precision data, $M_H = 89^{+42}_{-30}$ GeV at 68% confidence level [23]¹. The Tevatron with an integrated luminosity of 6 fb⁻¹ will be able to exclude a Higgs boson with 115 GeV < M_H < 180 GeV at 95% confidence level [24], which will provide important guidance for the search strategy at the CERN Large Hadron Collider. Thus, to fully exploit the Tevatron's potential to detect the SM Higgs boson or to impose limits on its mass, it is crucial that the dominant background processes are under good theoretical control.

In the present experimental analyses² the effects of NLO QCD corrections on the total cross-section and the dijet invariant mass distribution of the $Wb\bar{b}$ background process have been taken into account by using the MCFM package [25]. In MCFM, the NLO QCD predictions of both total and differential cross-sections for the $q\bar{q}' \rightarrow Wb\bar{b}$ production process have been calculated in the zero bottom-quark mass ($m_b = 0$) approximation [26, 27]. From a study of the Leading Order (LO) cross-section, finite bottom-quark mass effects are expected

¹ For an update see the LEPWWG website at <http://lepewwg.web.cern.ch/LEPEWWG>

² For updated results, see the CDF and DØ websites at www-cdf.fnal.gov/physics/exotic/exotic.html and www-d0.fnal.gov/Run2Physics/WWW/results/higgs.htm.

to affect both total and differential $Wb\bar{b}$ cross-sections mostly in the region of small $b\bar{b}$ -pair invariant masses [27]. Given the variety of experimental analyses involved both in the search for HW associated production and single-top production, it is important to precisely assess the impact of a finite bottom-quark mass over the entire kinematical reach of the process, including complete NLO QCD corrections.

In this paper we compute the NLO QCD corrections to $q\bar{q}' \rightarrow Wb\bar{b}$, including full bottom-quark mass effects. Using the MCFM package [25], we compare our results with the corresponding results obtained in the $m_b = 0$ limit. Numerical results are presented for the total cross-section and the invariant mass distribution of the $b\bar{b}$ jet pair, for the Tevatron $p\bar{p}$ collider, including kinematic cuts and a jet-finding algorithm. In particular, we apply the k_T jet algorithm and require two tagged b -jets in the final state.

The outline of the paper is as follows. In Section II we briefly discuss the technical details of our calculation, while we present numerical results and a discussion of the bottom-quark mass effects in Section III. Section IV contains our conclusions.

II. CALCULATION

The NLO QCD corrections to $q\bar{q}' \rightarrow b\bar{b}W$ consist of both one-loop virtual corrections to the tree level processes depicted in Fig. 1 and one-parton real radiation from both the initial and final state quarks, i.e. $q\bar{q}' \rightarrow b\bar{b}W + g$. At the same order, the $qg(\bar{q}g) \rightarrow b\bar{b}W + q(\bar{q})$ process also needs to be included.

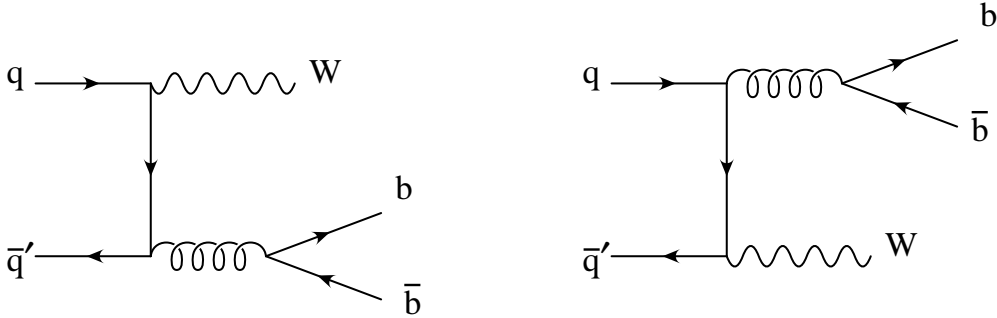


FIG. 1: Tree level Feynman diagrams for $q\bar{q}' \rightarrow b\bar{b}W$.

The $O(\alpha_s)$ virtual corrections consist of self-energy, vertex, box, and pentagon diagrams with several massive propagators, since we take $m_b \neq 0$. They contain both UV and IR

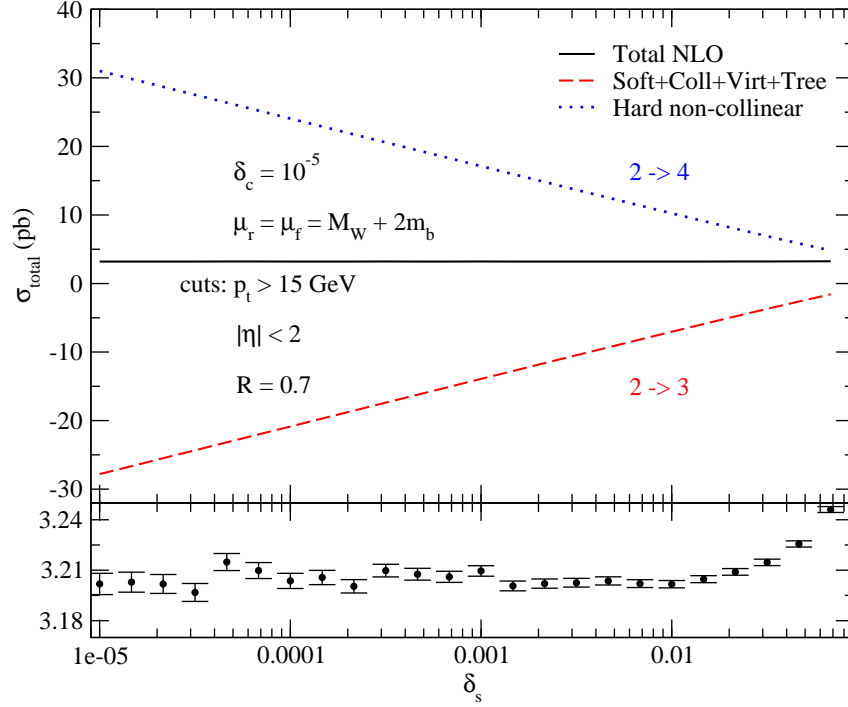


FIG. 2: Dependence of the total NLO QCD cross-section on the δ_s PSS parameter, when δ_c is fixed at $\delta_c = 10^{-5}$. In the upper window we illustrate separately the cutoff dependence of the soft and hard-collinear part ($2 \rightarrow 3$, red dashed curve) and of the hard non-collinear part ($2 \rightarrow 4$, blue dotted curve) of the real corrections to the total cross-section. The $2 \rightarrow 3$ curve also includes those parts of the $2 \rightarrow 3$ NLO cross-section that do not depend on δ_c and δ_s , i.e. the tree level and one-loop virtual contributions. The sum of all the contributions corresponds to the black solid line. The lower window shows a blow-up of the black solid line in the upper plot, to illustrate the stability of the result. The error bars indicate the statistical uncertainty of the Monte Carlo integration.

singularities which need to be computed analytically. For box and pentagon diagrams we use techniques similar to the ones explained in detail in Refs. [28, 29]. We use dimensional regularization with $d = 4 - 2\epsilon$, and extract both UV and IR divergences as poles in ϵ . The UV singularities are cancelled by introducing a suitable series of counterterms. We renormalize the wave functions of the external quark fields in the on-shell scheme, and the strong coupling constant α_s in the \overline{MS} -scheme, decoupling the top quark. At this order in QCD the weak

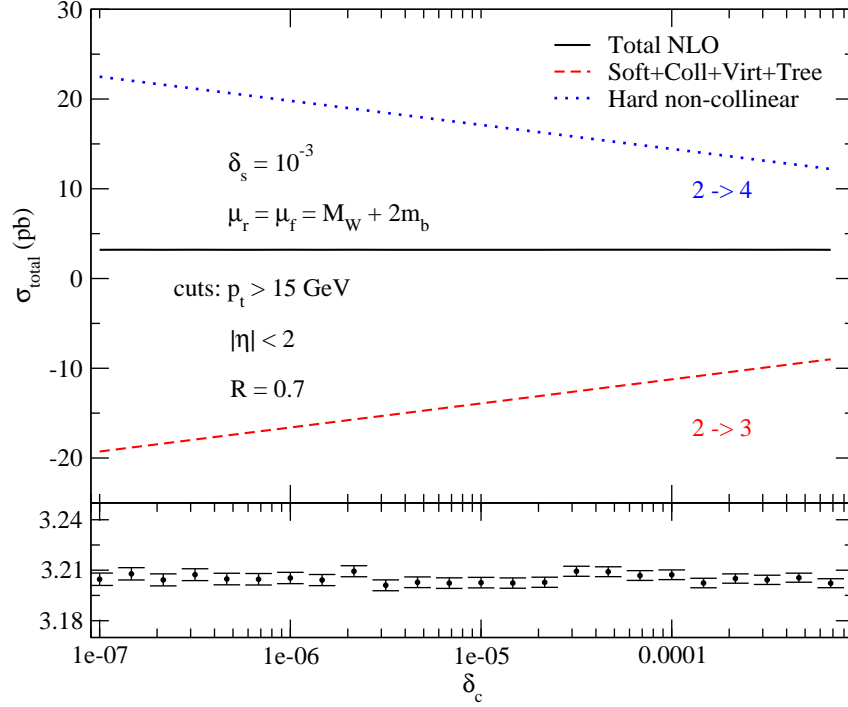


FIG. 3: Dependence of the total NLO QCD cross-section on the δ_c PSS parameter, when δ_s is fixed at $\delta_s = 10^{-3}$. In the upper window we illustrate separately the cutoff dependence of the soft and hard-collinear part ($2 \rightarrow 3$, red dashed curve) and of the hard non-collinear part ($2 \rightarrow 4$, blue dotted curve) of the real corrections to the total cross-section. The $2 \rightarrow 3$ curve also includes those parts of the $2 \rightarrow 3$ NLO cross-section that do not depend on δ_c and δ_s , i.e. the tree level and one-loop virtual contributions. The sum of all the contributions corresponds to the black solid line. The lower window shows a blow-up of the black solid line in the upper plot, to illustrate the stability of the result. The error bars indicate the statistical uncertainty of the Monte Carlo integration.

vertex renormalization consists only of the external quark wave-function renormalization. Self-energy, vertex, box, and pentagon diagrams contain IR divergences that combine and cancel against the analogous divergences in the real emission $O(\alpha_s)$ corrections, and in the renormalized Parton Distribution Functions (PDF).

We compute the real emission $O(\alpha_s)$ corrections using the Phase Space Slicing (PSS) method with two cutoffs: δ_s for the soft singularities, and δ_c for the hard-collinear singu-

larities [28, 29, 30]. The independence of the final result on the arbitrary values of δ_s and δ_c has been checked over a large range of values for both parameters and is illustrated in Figs. 2 and 3. The numerical results in Section III have been obtained using $\delta_s = 10^{-3}$ and $\delta_c = 10^{-5}$.

In our calculation we treat γ_5 according to the naive dimensional regularization approach, i.e. we enforce that γ_5 anticommutes with all other γ matrices in $d = 4 - 2\epsilon$ dimensions. This is known to give origin to inconsistencies when at the same time the d -dimensional trace of four γ matrices and one γ_5 is forced to be non-zero (as in $d = 4$, where $Tr(\gamma^\mu \gamma^\nu \gamma^\rho \gamma^\sigma \gamma_5) = 4i\epsilon^{\mu\nu\rho\sigma}$) [31]. In our calculation both UV and IR divergences are handled in such a way that we never have to enforce simultaneously these two properties of the Dirac algebra in d dimensions. For instance, the UV divergences are extracted and cancelled at the amplitude level, after which the $d \rightarrow 4$ limit is taken and the renormalized amplitude is squared using $d = 4$. Thus, all fermion traces appearing at this point are computed in four dimensions and therefore have no ambiguities.

Both virtual and real corrections have been checked by independent calculations that have used FORM [32], TRACER [33], the FF package [34], and MAPLE. The $2 \rightarrow 4$ amplitudes for the real corrections have been double checked using Madgraph [35, 36, 37].

III. NUMERICAL RESULTS

In this paper we present results for $Wb\bar{b}$ production at the Tevatron, including NLO QCD corrections, and using a non-zero bottom-quark mass, fixed at $m_b = 4.62$ GeV. The W boson is considered on-shell and its mass is taken to be $M_W = 80.41$ GeV. The mass of the top quark, entering in virtual corrections, is set to $m_t = 174$ GeV. The LO results use the 1-loop evolution of α_s and the CTEQ6L set of PDF [38], while the NLO results use the 2-loop evolution of α_s and the CTEQ6M set of PDF, with $\alpha_s^{NLO}(M_Z) = 0.118$. The W boson coupling to quarks is proportional to the Cabibbo-Kobayashi-Maskawa (CKM) matrix elements. We take $V_{ud} = V_{cs} = 0.975$ and $V_{us} = V_{cd} = 0.222$, while we neglect the contribution of the third generation, since it is suppressed either by the initial state quark densities or by the corresponding CKM matrix elements.

We implement the k_T jet algorithm [39, 40, 41, 42] with a pseudo-cone size $R = 0.7$ and we recombine the parton momenta within a jet using the so called covariant E -scheme [40]. We

checked that our implementation of the k_T jet algorithm coincides with the one in MCFM. We require all events to have a $b\bar{b}$ jet pair in the final state, with a transverse momentum larger than 15 GeV ($p_T^{b,\bar{b}} > 15$ GeV) and a pseudorapidity that satisfies $|\eta^{b,\bar{b}}| < 2$. We impose the same p_T and $|\eta|$ cuts also on the extra jet that may arise due to hard non-collinear real emission of a parton, i.e. in the processes $Wb\bar{b} + g$ or $Wb\bar{b} + q(\bar{q})$. This hard non-collinear extra parton is treated either *inclusively* or *exclusively*, following the definition of *inclusive* and *exclusive* as implemented in the MCFM code [25]. In the *inclusive* case we include both two- and three-jet events, while in the *exclusive* case we require exactly two jets in the event. Two-jet events consist of a bottom-quark jet pair that may also include a final-state light parton (gluon or quark) due to the applied recombination procedure. Results in the massless bottom-quark approximation have been obtained using the MCFM code [25].

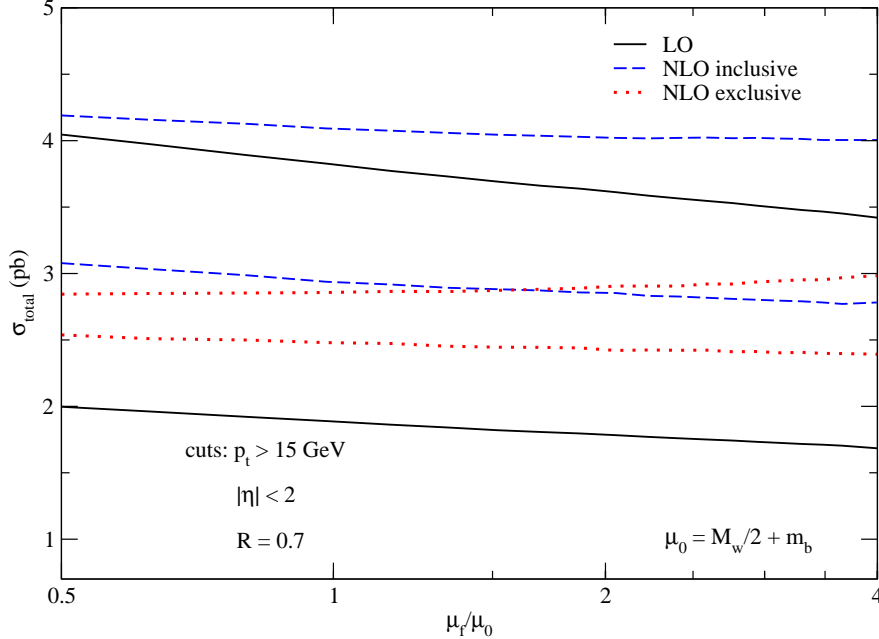


FIG. 4: Dependence of the LO (black solid band), NLO *inclusive* (blue dashed band), and NLO *exclusive* (red dotted band) total cross-sections on the renormalization/factorization scales, including full bottom-quark mass effects. The bands are obtained by varying both μ_R and μ_F between $\mu_0/2$ and $4\mu_0$ (with $\mu_0 = m_b + M_W/2$).

In Figs. 4-6 we illustrate the renormalization and factorization scale dependence of the LO and NLO total cross-sections, both in the *inclusive* and *exclusive* case. Fig. 4 shows the overall scale dependence of both LO, NLO *inclusive* and NLO *exclusive* total cross-

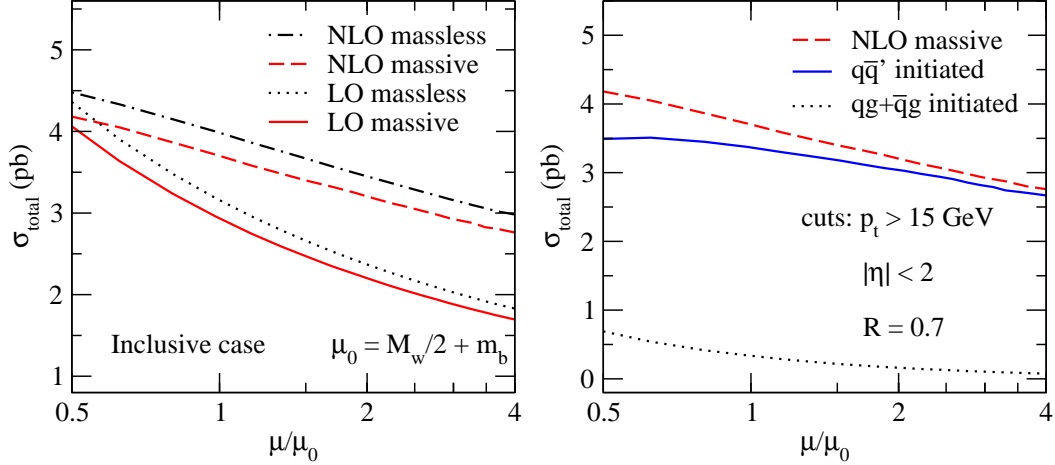


FIG. 5: Dependence of the LO and NLO *inclusive* total cross-section on the renormalization/factorization scale, when $\mu_R = \mu_F$. The left hand side plot compares both LO and NLO total cross-sections for the case in which the bottom quark is treated as massless (MCFM) or massive (our calculation). The right hand side plot shows separately, for the massive case only, the scale dependence of the $q\bar{q}'$ and $qg + \bar{q}g$ contributions, as well as their sum.

sections, when both μ_R and μ_F are varied independently between $\mu_0/2$ and $4\mu_0$ (with $\mu_0 = m_b + M_W/2$), including full bottom-quark mass effects. We notice that the NLO cross-sections have a reduced scale dependence over most of the range of scales shown, and the *exclusive* NLO cross-section is more stable than the *inclusive* one especially at low scales. This is consistent with the fact that the *inclusive* NLO cross-section integrates over the entire phase space of the $qg(\bar{q}g) \rightarrow b\bar{b}W + q(\bar{q})$ channels that are evaluated with NLO α_s and NLO PDF, but are actually tree-level processes and retain therefore a strong scale dependence. In the *exclusive* case only the $2 \rightarrow 3$ collinear kinematic of these processes is retained, since 3-jets events are discarded, and this makes the overall renormalization and factorization scale dependence milder. To better illustrate this point, we show in the right hand side plots of Figs. 5 and 6 the mu-dependence of the total cross section and of the partial cross-sections corresponding to the $q\bar{q}'$ and the $qg + \bar{q}g$ initiated channels separately, for $\mu_R = \mu_F$, both for the *inclusive* and for the *exclusive* case. It is clear that the low scale instability of the *inclusive* cross-section is entirely driven by the $qg + \bar{q}g$ contribution. In the left hand side plots of Figs. 5 and 6 we also compare the scale dependence of our results to the scale dependence of the corresponding results obtained with $m_b = 0$ (using MCFM),

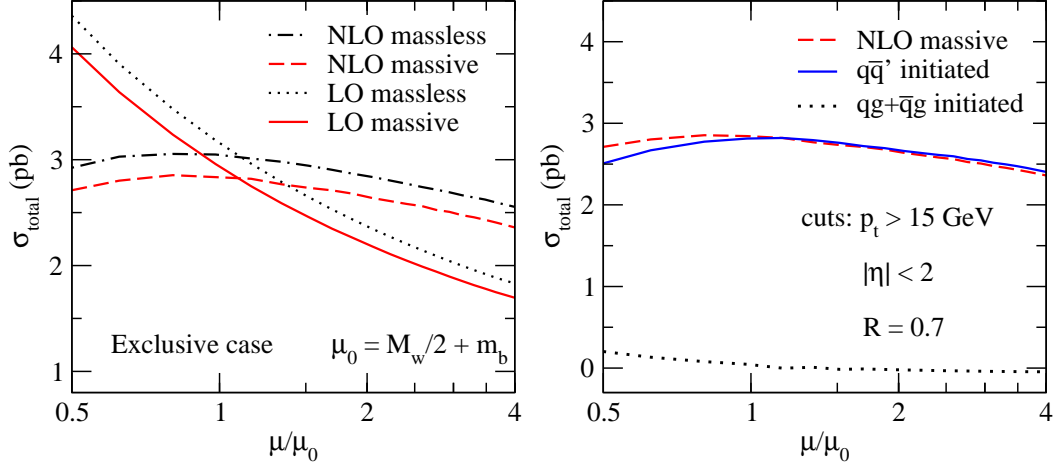


FIG. 6: Dependence of the LO and NLO *exclusive* total cross-section on the renormalization/factorization scale, when $\mu_R = \mu_F$. The left hand side plot compares both LO and NLO total cross-sections for the case in which the bottom quark is treated as massless (MCFM) or massive (our calculation). The right hand side plot shows separately, for the massive case only, the scale dependence of the $q\bar{q}'$ and $qg + \bar{q}g$ contributions, as well as their sum.

both at LO and at NLO. Using a non-zero value of m_b is not expected to have any impact on the scale dependence of the result³ and, indeed, the scale dependence of the LO and NLO pair of curves is very similar, with a shift due to the bottom-quark mass effects.

While the LO cross-section still has a 40% uncertainty due to scale dependence, this uncertainty is reduced at NLO to about 20% for the *inclusive* and to about 10% for the *exclusive* cross-section respectively. The uncertainties have been estimated as the positive/negative deviation with respect to the mid-point of the bands plotted in Fig. 4, where each band range is defined by the minimum and maximum value in the band. We notice incidentally that the difference due to finite bottom-quark mass effects is less significant than the theoretical uncertainty due to the residual scale dependence in the *inclusive* case, but is comparable in size in the *exclusive* case. Indeed, the finite bottom-quark mass effects amount to about 8% in both *inclusive* and *exclusive* cases.

In Fig. 7 we show the rescaled difference between the total cross-sections obtained from

³ Note that we always use $m_b = 4.62$ GeV in the determination of the scales in terms of $\mu_0 = m_b + M_W/2$ even in the results obtained with $m_b = 0$.

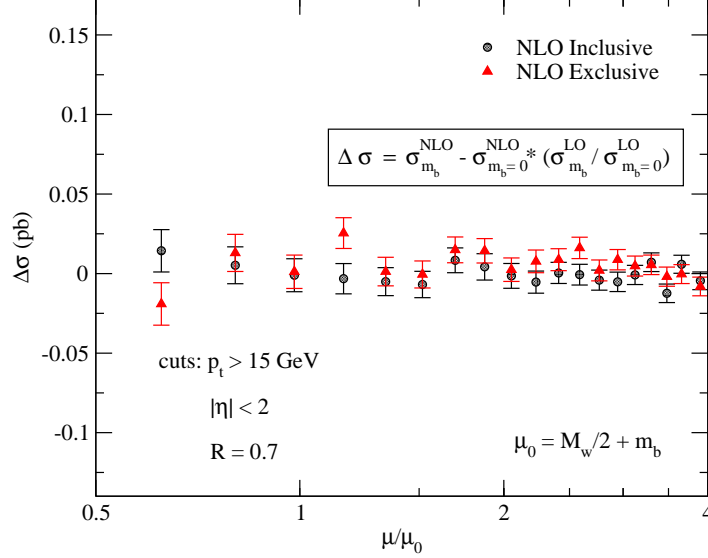


FIG. 7: Dependence on the renormalization/factorization scale of the rescaled difference between our NLO calculation (with $m_b \neq 0$) of the total cross-section and MCFM (with $m_b = 0$) for the *inclusive* and *exclusive* cases (with $\mu_R = \mu_F$). The error bars indicate the statistical uncertainty of the Monte Carlo integration.

our calculation (with $m_b \neq 0$) and with MCFM (with $m_b = 0$) defined as follows:

$$\Delta\sigma = \sigma^{NLO}(m_b \neq 0) - \sigma^{NLO}(m_b = 0) \frac{\sigma^{LO}(m_b \neq 0)}{\sigma^{LO}(m_b = 0)}.$$

As can be seen, within the statistical errors of the Monte Carlo integration, the finite bottom-quark mass effects on the total cross-sections at NLO are well described by the corresponding effects at LO.

Finally, in Figs. 8-12 we study the distribution $d\sigma/dm_{b\bar{b}}$, where $m_{b\bar{b}}$ is the invariant mass of the $b\bar{b}$ jet pair. The impact of NLO QCD corrections on this distribution is illustrated in Figs. 8 and 9 for the *inclusive* and *exclusive* case respectively. We see that the NLO QCD corrections affects the cross section quite substantially in particular for low values of $m_{b\bar{b}}$. In each figure the right hand side plot gives the ratio of the NLO and LO distributions, providing a sort of K -factor bin by bin. Figs. 10 and 11 compare the NLO $d\sigma/dm_{b\bar{b}}$ distributions obtained from the massive and massless bottom-quark calculations. The results with $m_b = 0$ have been obtained using MCFM. As expected, most of the difference between the massless and massive bottom-quark cross-sections is coming from the region of low invariant mass $m_{b\bar{b}}$, both at LO and at NLO, where the cross-sections for $m_b \neq 0$ are consistently below the

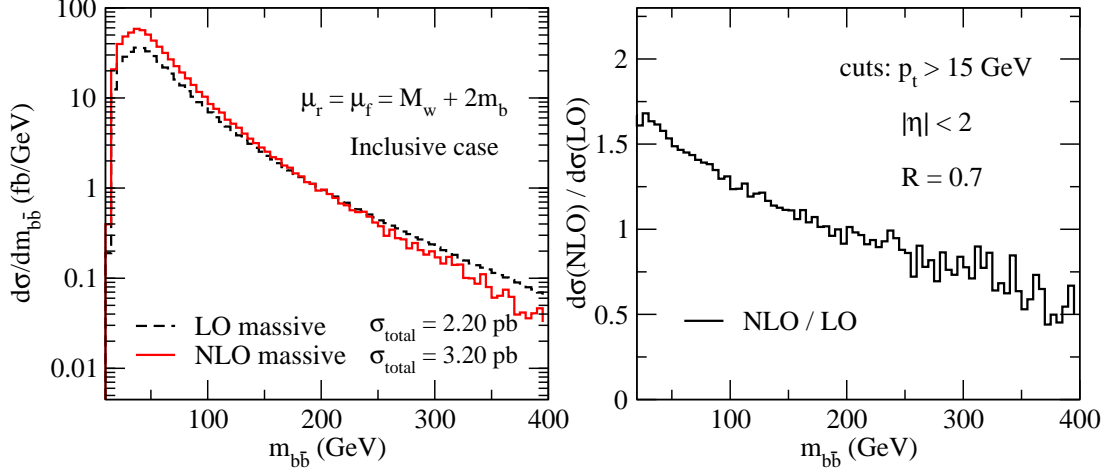


FIG. 8: The *inclusive* distribution $d\sigma/dm_{b\bar{b}}$ in LO and NLO QCD. The right hand side plot shows the ratio of the LO and NLO distributions.

ones with $m_b = 0$. For completeness, we also show in Fig. 12 the comparison between massive ($m_b \neq 0$) and massless ($m_b = 0$) calculations at LO in QCD. The LO $m_{b\bar{b}}$ distribution for massive bottom-quarks has been obtained both from our calculation and from MCFM, which implements the $m_b \neq 0$ option at tree level, and both results have been found in perfect agreement. As can be seen by comparing Figs. 10-11 and Fig. 12, the impact of a non-zero bottom-quark mass is almost not affected by including NLO QCD corrections. To illustrate this in more detail we show in Fig. 13 the rescaled difference between the $m_{b\bar{b}}$ distributions obtained with our NLO calculation (with $m_b \neq 0$) and with MCFM (with $m_b = 0$) defined as follows:

$$\Delta \frac{d\sigma}{dm_{b\bar{b}}} = \frac{d\sigma^{NLO}}{dm_{b\bar{b}}}(m_b \neq 0) - \frac{d\sigma^{NLO}}{dm_{b\bar{b}}}(m_b = 0) \frac{d\sigma^{LO}(m_b \neq 0)}{d\sigma^{LO}(m_b = 0)}.$$

Apart from small deviations in the $m_{b\bar{b}}$ region below about 100 GeV, the finite bottom-quark mass effects at NLO are well described by the LO calculations.

IV. CONCLUSIONS

We have calculated the NLO QCD corrections to $q\bar{q}' \rightarrow Wb\bar{b}$ production including full bottom-quark mass effects. We have presented numerical results for the total cross-section

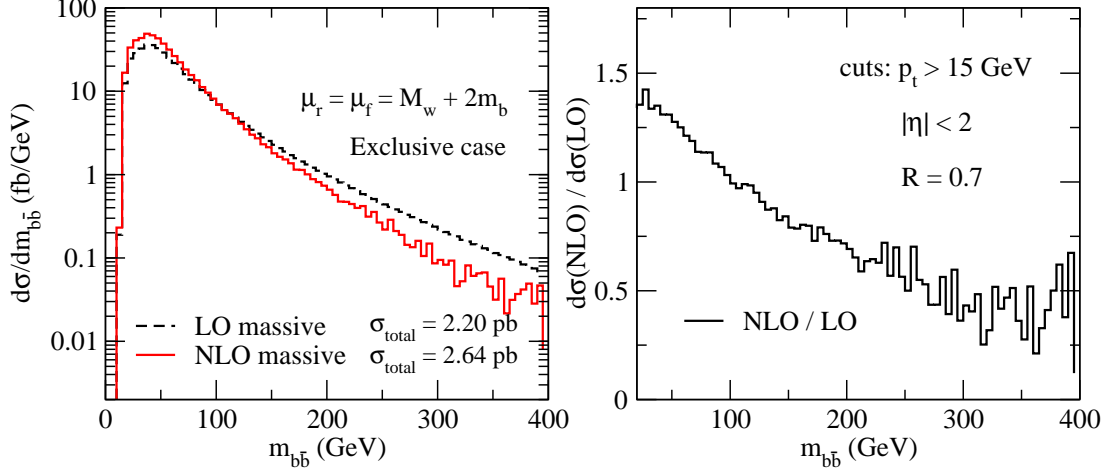


FIG. 9: The *exclusive* distribution $d\sigma/dm_{b\bar{b}}$ in LO and NLO QCD. The right hand side plot shows the ratio of the LO and NLO distributions.

and the invariant mass distribution of the bottom-quark jet pair ($m_{b\bar{b}}$) at the Tevatron for both massless and massive bottom quarks. We apply the k_T jet algorithm, require two b -tagged jets, and impose kinematical cuts that are inspired by the $D\bar{0}$ and CDF searches for the SM Higgs boson in WH production. The bottom-quark mass effects amount to about 8% of the total NLO QCD cross-section and can impact the shape of the $m_{b\bar{b}}$ distributions, in particular in regions of low $m_{b\bar{b}}$. This is relevant to SM Higgs searches in WH associated production and to searches for single-top production.

-
- [1] A. Abulencia et al. (CDF), Phys. Rev. Lett. **96**, 081803 (2006), hep-ex/0512051.
 - [2] CDF Note 8240 (2006).
 - [3] V. M. Abazov et al. (D0), Phys. Rev. Lett. **94**, 091802 (2005), hep-ex/0410062.
 - [4] $D\bar{0}$ Notes 4896-CONF and 5054-CONF (2006).
 - [5] A. Patwa (for the CDF and $D\bar{0}$ collaborations) (2006), hep-ex/0605082.
 - [6] D. Acosta et al. (CDF), Phys. Rev. **D71**, 012005 (2005), hep-ex/0410058.
 - [7] V. M. Abazov et al. (D0), Phys. Lett. **B622**, 265 (2005), hep-ex/0505063.
 - [8] A. Gresele (for the CDF and $D\bar{0}$ collaborations) (2006), hep-ex/0605041.

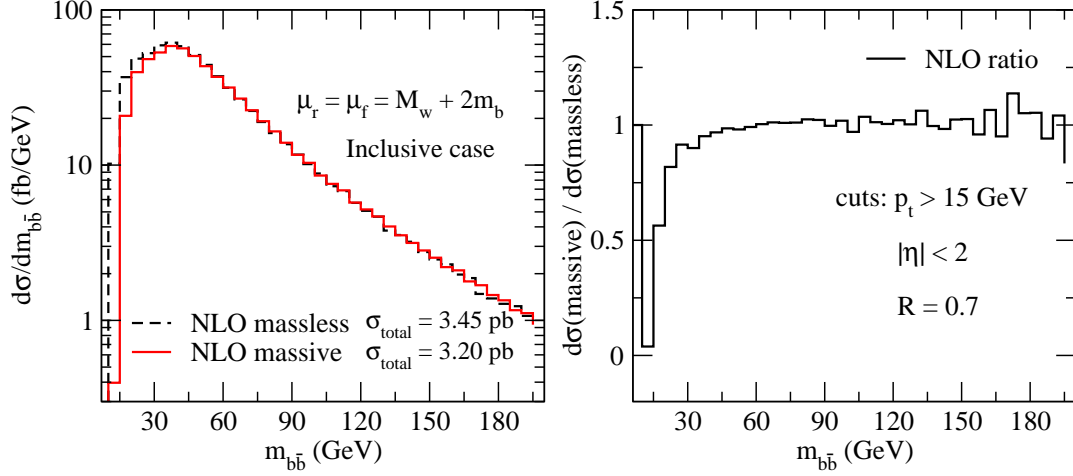


FIG. 10: The *inclusive* distribution $d\sigma/dm_{b\bar{b}}$ derived from our calculation (with $m_b \neq 0$) and from MCFM (with $m_b = 0$). The right hand side plot shows the ratio of the two distributions, $d\sigma(m_b \neq 0)/d\sigma(m_b = 0)$.

- [9] T. Han and S. Willenbrock, Phys. Lett. **B273**, 167 (1991).
- [10] S. Mrenna and C. P. Yuan, Phys. Lett. **B416**, 200 (1998), hep-ph/9703224.
- [11] O. Brein, A. Djouadi, and R. Harlander, Phys. Lett. **B579**, 149 (2004), hep-ph/0307206.
- [12] M. L. Ciccolini, S. Dittmaier, and M. Krämer, Phys. Rev. **D68**, 073003 (2003), hep-ph/0306234.
- [13] T. Stelzer, Z. Sullivan, and S. Willenbrock, Phys. Rev. **D56**, 5919 (1997), hep-ph/9705398.
- [14] T. Stelzer, Z. Sullivan, and S. Willenbrock, Phys. Rev. **D58**, 094021 (1998), hep-ph/9807340.
- [15] M. C. Smith and S. Willenbrock, Phys. Rev. **D54**, 6696 (1996), hep-ph/9604223.
- [16] B. W. Harris, E. Laenen, L. Phaf, Z. Sullivan, and S. Weinzierl, Phys. Rev. **D66**, 054024 (2002), hep-ph/0207055.
- [17] Z. Sullivan, Phys. Rev. **D70**, 114012 (2004), hep-ph/0408049.
- [18] Z. Sullivan, Phys. Rev. **D72**, 094034 (2005), hep-ph/0510224.
- [19] Q.-H. Cao and C. P. Yuan, Phys. Rev. **D71**, 054022 (2005), hep-ph/0408180.
- [20] Q.-H. Cao, R. Schwienhorst, and C. P. Yuan, Phys. Rev. **D71**, 054023 (2005), hep-ph/0409040.
- [21] Q.-H. Cao, R. Schwienhorst, J. A. Benitez, R. Brock, and C. P. Yuan, Phys. Rev. **D72**, 094027

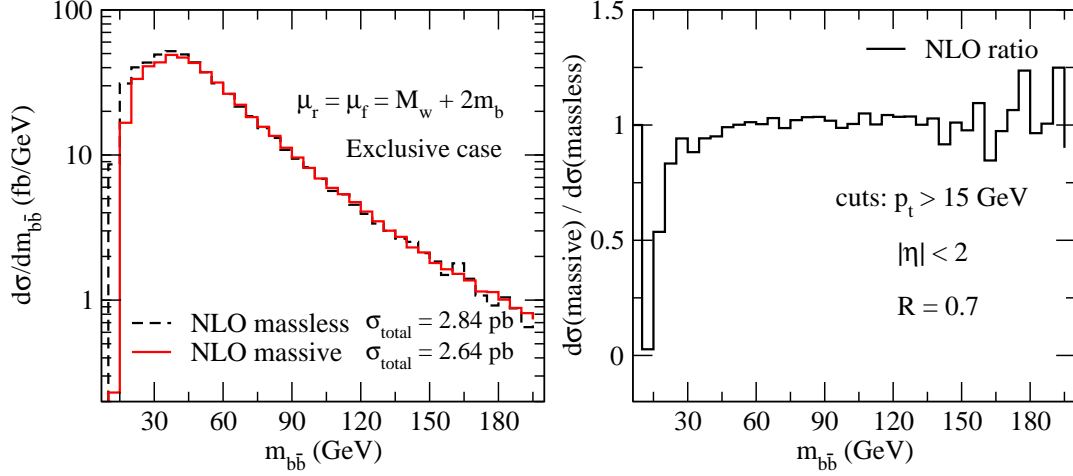


FIG. 11: The *exclusive* distribution $d\sigma/dm_{b\bar{b}}$ derived from our calculation (with $m_b \neq 0$) and from MCFM (with $m_b = 0$). The right hand side plot shows the ratio of the two distributions, $d\sigma(m_b \neq 0)/d\sigma(m_b = 0)$.

(2005), hep-ph/0504230.

- [22] M. Beccaria, G. Macorini, F. M. Renard, and C. Verzegnassi (2006), hep-ph/0605108.
- [23] ALEPH, DELPHI, L3, OPAL, and LEPWWG (2005), hep-ex/0511027.
- [24] L. Sonnenschein, talk given at HCP 2006, <http://hcp2006.phy.duke.edu>.
- [25] J. Campbell and R. Ellis, webpage: mcfm.fnal.gov.
- [26] R. K. Ellis and S. Veseli, Phys. Rev. **D60**, 011501(R) (1999), hep-ph/9810489.
- [27] J. Campbell and R. K. Ellis, Phys. Rev. **D65**, 113007 (2002), hep-ph/0202176.
- [28] L. Reina, S. Dawson, and D. Wackeroth, Phys. Rev. **D65**, 053017 (2002), hep-ph/0109066.
- [29] S. Dawson, C. Jackson, L. H. Orr, L. Reina, and D. Wackeroth, Phys. Rev. **D68**, 034022 (2003), hep-ph/0305087.
- [30] B. W. Harris and J. F. Owens, Phys. Rev. **D65**, 094032 (2002), hep-ph/0102128.
- [31] S. A. Larin, Phys. Lett. **B303**, 113 (1993), hep-ph/9302240.
- [32] J. A. M. Vermaseren (2000), math-ph/0010025.
- [33] M. Jamin and M. E. Lautenbacher, Comput. Phys. Commun. **74**, 265 (1993).
- [34] G. J. van Oldenborgh, Comput. Phys. Commun. **66**, 1 (1991).

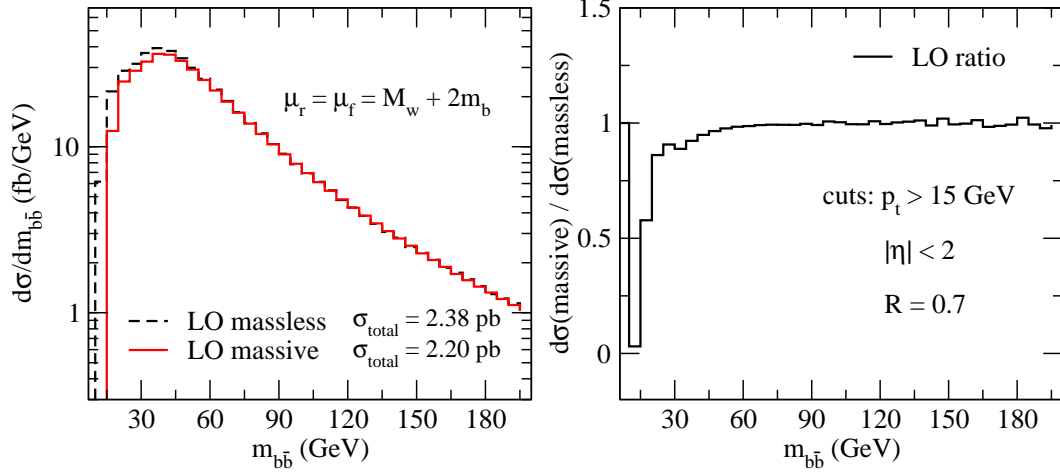


FIG. 12: The LO distribution $d\sigma/dm_{b\bar{b}}$ derived from our calculation (with $m_b \neq 0$) and from MCFM (with $m_b = 0$). The right hand side plot shows the ratio of the two distributions, $d\sigma(m_b \neq 0)/d\sigma(m_b = 0)$.

- [35] H. Murayama, I. Watanabe, and K. Hagiwara (1992), kEK-91-11.
- [36] T. Stelzer and W. F. Long, Comput. Phys. Commun. **81**, 357 (1994), hep-ph/9401258.
- [37] F. Maltoni and T. Stelzer, JHEP **02**, 027 (2003), hep-ph/0208156.
- [38] H. L. Lai et al. (CTEQ), Eur. Phys. J. **C12**, 375 (2000), hep-ph/9903282.
- [39] S. Catani, Y. L. Dokshitzer, and B. R. Webber, Phys. Lett. **B285**, 291 (1992).
- [40] S. Catani, Y. L. Dokshitzer, M. H. Seymour, and B. R. Webber, Nucl. Phys. **B406**, 187 (1993).
- [41] S. D. Ellis and D. E. Soper, Phys. Rev. **D48**, 3160 (1993), hep-ph/9305266.
- [42] W. B. Kilgore and W. T. Giele, Phys. Rev. **D55**, 7183 (1997), hep-ph/9610433.

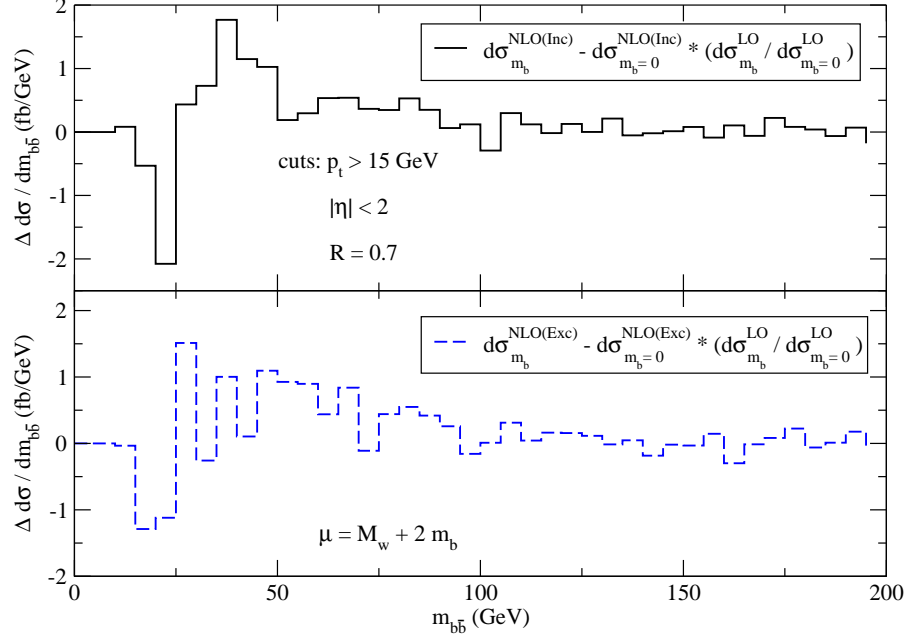


FIG. 13: The $m_{b\bar{b}}$ distribution of the rescaled difference between our NLO calculation (with $m_b \neq 0$) and MCFM (with $m_b = 0$) for the *inclusive* (upper plot) and *exclusive* case (lower plot).